Acta Geochim (2025) 44:1276–1292
https://doi.org/10.1007/s11631-025-00777-8

ORIGINAL ARTICLE

Arsenopyrite reveals the deuteric origin of the Saxi tungsten deposit, SW China

Wanbo Li[1,2] · **Mingguo Deng**[1,2] · **Qiang Weng**[1,2] · **Wenchang Li**[1,2] · **Zhen Jia**[1,2] ·
Wenbo Song[1,2] · **Zhengrong Li**[1,2] · **Jiafei Yang**[3]

Received: 26 November 2024 / Revised: 11 March 2025 / Accepted: 24 March 2025 / Published online: 15 May 2025
© The Author(s), under exclusive licence to Science Press and Institute of Geochemistry, CAS and Springer-Verlag GmbH Germany, part of Springer Nature 2025

Abstract The Saxi tungsten deposit, located in the Laojunshan ore district of southeastern Yunnan Province, is a significant W-polymetallic deposit. The origins of tungsten-bearing pegmatite dikes and quartz vein mineralization in the Saxi deposit remain poorly understood. This study employs in situ U–Pb dating of apatite from the altered granite, along with trace element and S–Pb isotopic analysis of arsenopyrite, to investigate the timing, source of ore-forming fluids and the mechanisms of tungsten enrichment. The apatite in the altered granite yields a U–Pb age of 147.0±4.0 Ma, indicating magmatic activity during the Early Cretaceous. Three generations of arsenopyrite (Apy) are identified: Apy-1 in the altered granite, Apy-2 in the pegmatite dikes and Apy-3 in the quartz veins. The S/Fe ratios for Apy-1, Apy-2 and Apy-3 range from 0.98 to 1.09, 0.89 to 0.92 and 0.86 to 1.02, respectively (average 0.97), suggesting a magmatic-hydrothermal origin. Sulfur isotope values ($\delta^{34}S = 4.29‰–8.11‰$) indicate that it was likely sourced from deep magmatic-hydrothermal fluids. Lead isotopic compositions of arsenopyrite suggest that the granitic parental magma is derived from the upper crust. These findings point to a magmatic-hydrothermal origin for the vein-type tungsten mineralization, linked to a concealed magmatic-hydrothermal system in the Early Cretaceous.

Keywords Three arsenopyrite generations · Deuteric origin · Tungsten enrichment *in-situ* arsenopyrite trace elements and S–Pb isotopes · Saxi deposit

1 Introduction

Tungsten is a critical and strategic metal, having the highest melting point of all non-alloyed metals, with widespread applications in the aerospace, automotive, electronic and defense industries (Wu et al. 2023). To our knowledge, tungsten mineralization is typically associated with granitic magmatic-hydrothermal and metamorphic processers (e.g., Poulin et al. 2016; Chai et al. 2023; Li et al. 2023). Global tungsten deposits are mainly concentrated in the

---

Supplementary Information The online version contains supplementary material available at https://doi.org/10.1007/s11631-025-00777-8.

✉ Mingguo Deng
minguod@kust.edu.cn

✉ Qiang Weng
wengqiang1234@outlook.com

Wanbo Li
2838971925@qq.com

Wenchang Li
20200123@kust.edu.cn

Zhen Jia
zhenjia0514@163.com

Wenbo Song
504238367@qq.com

Zhengrong Li
2927582308@qq.com

Jiafei Yang
752538461@qq.com

[1] Faculty of Land Resource Engineering, Kunming University of Science and Technology, Kunming 650093, China

[2] Key Laboratory of Sanjiang Metallogeny and Resources Exploration and Utilization, Ministry of Natural Resources of the People's Republic of China, Kunming 650051, China

[3] Ecological Environment Geological Service Center of Henan Geological Bureau, Henan 450014, China

Alps-Himalayas and the Pacific Rim tectonic domains. Most of these tungsten deposits are closely related to granitic magmatic-hydrothermal processes, but some tungsten deposits are related to metamorphic process such as the Mactung deposit in Canada (Elongo et al. 2020) and the Watershed deposit in Australia (Poblete et al. 2021). Notably, both magmatic and metamorphic tungsten deposits consist of vein-type orebodies. Effectively identifying the genesis of the vein-type tungsten mineralization has significant implications for mineral exploration.

Numerous tungsten deposits have been identified in the Laojunshan area of southeastern Yunnan Province, establishing it as a significant tungsten production base (Shi et al. 2015). The Saxi deposit, situated at the eastern margin of the Laojunshan pluton, represents a typical W–Be occurrence with many vein-type orebodies. This deposit has been influenced by a regional metamorphic event followed by magmatic-hydrothermal overprint (Zhang et al. 2012; Que et al. 2014), resulting in uncertainties concerning the genesis of the vein-type tungsten orebodies. Previous studies have primarily focused on the beryllium mineralization mechanism in this deposit (e.g., Xue et al. 2010; Zheng et al. 2019; Long et al. 2021), while investigations specifically addressing W mineralization remain limited. Most established work on scheelite has concentrated on metallogenic geochronology and the compositions of ore-forming fluids. Liu et al. (2011) and Que (2016) reported a ^{40}Ar-^{39}Ar age of 121 ± 4 Ma and 112.44 ± 0.77 Ma, respectively, for biotite in stratiform granulite from the Saxi deposit, suggesting an association with the late Yanshanian magmatic event. Zhang et al. (2016) examined fluid inclusions in both vein-type and stratiform orebodies, finding similar fluid properties in the two types, potentially indicating a shared source. Sheng (2016) and Sheng et al. (2023) analyzed H–O isotopes in quartz from the Saxi deposit, concluding that the ore-forming fluid was primarily magmatic in origin, with contributions from meteoric or formation water. In addition, Sheng (2016) analyzed sulfur isotopes of pyrite from quartz vein tungsten samples, which indicated a magmatic sulfur source, suggesting that the ore-forming fluids likely originated from magmatic-hydrothermal fluids. Although there is a general consensus linking the Saxi deposit to late Yanshanian magmatic-hydrothermal processes, the specific magmatic event remains unclear. Furthermore, due to the low closure temperature of the biotite Ar–Ar system, these ages may not accurately represent the tungsten metallogenic age. Thus, the genesis of the vein-type tungsten orebodies at the Saxi deposit remains controversial.

Three distinct occurrences of scheelite have been identified in the Saxi deposit, present in altered granite, pegmatite dikes and hydrothermal quartz veins. Analytical data for scheelite are currently under review by our team. Notably, the symbiotic association of arsenopyrite with scheelite is evident across the metallogenic process. The occurrence and in situ chemical composition of arsenopyrite, along with in situ S–Pb isotopic analyses provide critical insights into the sources of tungsten and ore-forming fluids in hydrothermal W deposits (e.g., Zartman and Doe 1981; Fleet et al. 1989; Cook and Chryssoulis 1990; Deditius et al. 2008; Large et al. 2009; Reich et al. 2013; Román et al. 2019; Wu et al. 2021). In this study, we integrated field and petrographic observations with LA-ICP-MS data from multistage arsenopyrite to investigate the evolution of the hydrothermal system. Additionally, in situ S–Pb isotopic analyses of arsenopyrite, conducted using LA-MC-ICP-MS, were employed to elucidate the sources of metals and ore-forming fluids. U–Pb dating of apatite in altered granite would further provide new insights into the genesis of the Saxi tungsten deposit.

2 Geological setting

2.1 Regional geology

The Saxi deposit is situated at the southwestern margin of the Yangtze Block (Fig. 1a) within the Laojunshan ore concentration area, a well-known tungsten polymetallic mining district in southeastern Yunnan Province (Fig. 1b; Zhang et al. 2016). This region lies at the intersection of the Indo-China Block, Yangtze Block and Cathaysia Block, forming part of the depression zone along the edge of the ancient Viet Bei landmass (Fig. 1a; Long et al. 2021). The area features a magmatic hot vault structure known as the Laojunshan-Song Chay Metamorphic Core Complex (L-S MCC), the most representative metamorphic-tectonic magmatic dome in the region. The L-S MCC comprises Caledonian and Yanshanian granites, Proterozoic Mengdong Group metamorphic rocks and Cambrian to Triassic sedimentary strata (Guo et al. 2009; Long et al. 2021). The core of the dome is primarily composed of Silurian gneissic granite and Late Cretaceous granite. Additionally, Proterozoic strata within the gneiss bedrock serve as the principal tungsten-bearing formations in the area (Zhang et al. 2016).

The study area and its surrounding regions underwent significant magmatic activity, which can be categorized into several key phases: Proterozoic, Silurian and Cretaceous (Que 2016). Among these, the Silurian and Cretaceous periods are particularly notable. Zircon U–Pb dating of exposed gneissic granite reveals magmatic crystallization ages between 427 and 436 Ma, corresponding to the Silurian magmatic event (Xu et al. 2016). The Laojunshan composite granitic pluton, emplaced during the Cretaceous, represents a multi-stage intrusive complex consisting predominantly of porphyritic granite, as evidenced by a broad range of zircon U–Pb ages from 117 to 83 Ma (Feng et al. 2010; Liu et al.

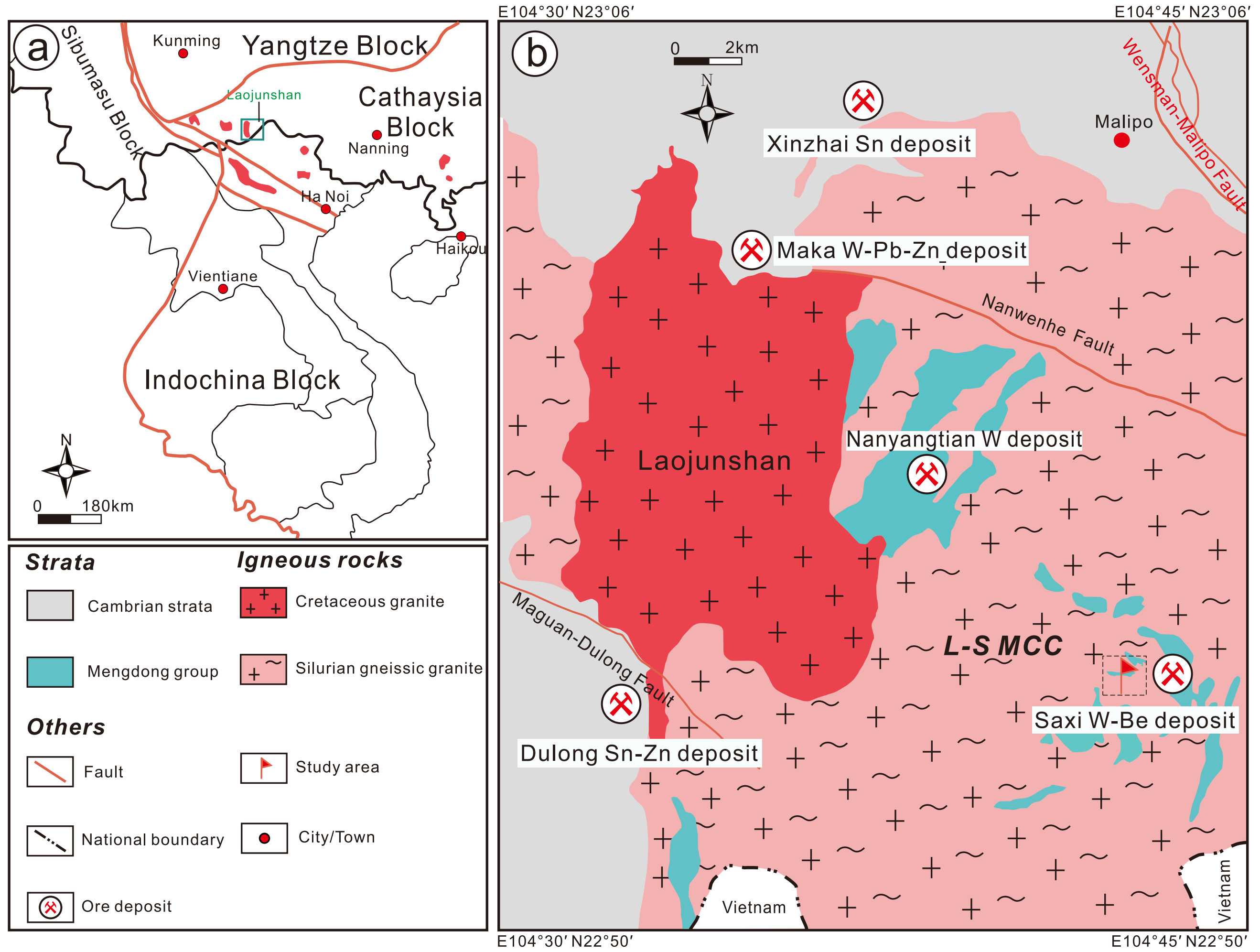

Fig. 1 **a** Location of the study area and the principal tectonic setting of present-day Southeast Asia; **b** geological sketch of the study area, modified from Zhang et al. (2012), Long et al. (2021); L-S MCC. Laojunshan-Song Shay Metamorphic Core Complex

2014; Lan et al. 2016). This granitic complex is spindle-shaped, approximately 17 km long and 10 km wide, with an exposed area of 153 km^2, exposed about 8 km northwest of the Saxi deposit (Fig. 1b; Long et al. 2021).

Several economic deposits are spatially adjacent to Cretaceous granite intrusions, including the Dulong Sn–Zn deposit (Wang et al. 2014) and Maka W–Pb–Zn deposit (Liu et al. 2023). In contrast, the Xinzhai Sn deposit (Feng et al. 2011a), Nanyangtian W deposit (Zhao et al. 2024) and Saxi W–Be deposit (Liu et al. 2011) are situated at a considerable distance from the Laojunshan granitic pluton (Fig. 1b).

2.2 Geology of the Saxi deposit

The primary exposed strata in the Saxi deposit consist of the metamorphic Mengdong Group, which includes the Saxi Formation and the Nanyangtian Formation. The Saxi Formation can be further subdivided into upper, middle and lower numbers (Fig. 2a; Que 2016). The tungsten orebodies are dominantly hosted within the middle number of the Saxi Formation (Fig. 2). Tungsten mineralization mainly occurs in vein-type ore bodies, which are composed mainly of pegmatite dikes and quartz veins that occur along or crosscut the stratigraphic layers.

According to the Mineral Resource Summary Report of Malipo Jinwei Mineral Co. Ltd., in June 2020, the Saxi Mining Area contains a total metal content (WO_3) of 59 352.06 tons. This includes industrial ore reserves of 9.5129 million tons with a WO_3 metal content of 58 479.24 tons, averaging a grade of 0.57%. The Saxi tungsten deposit has reached the scale of a large-scale deposit overall, demonstrating significant economic potential.

The orebodies are structurally controlled by the Jiaozishan syncline, with a synclinal axis oriented between 120° and 290° (Sheng et al. 2023). The core of the syncline consists of the upper member of the Saxi Formation, while the two flanks are represented by the middle and lower members (Sheng 2016). Underlying the Saxi Formation is the

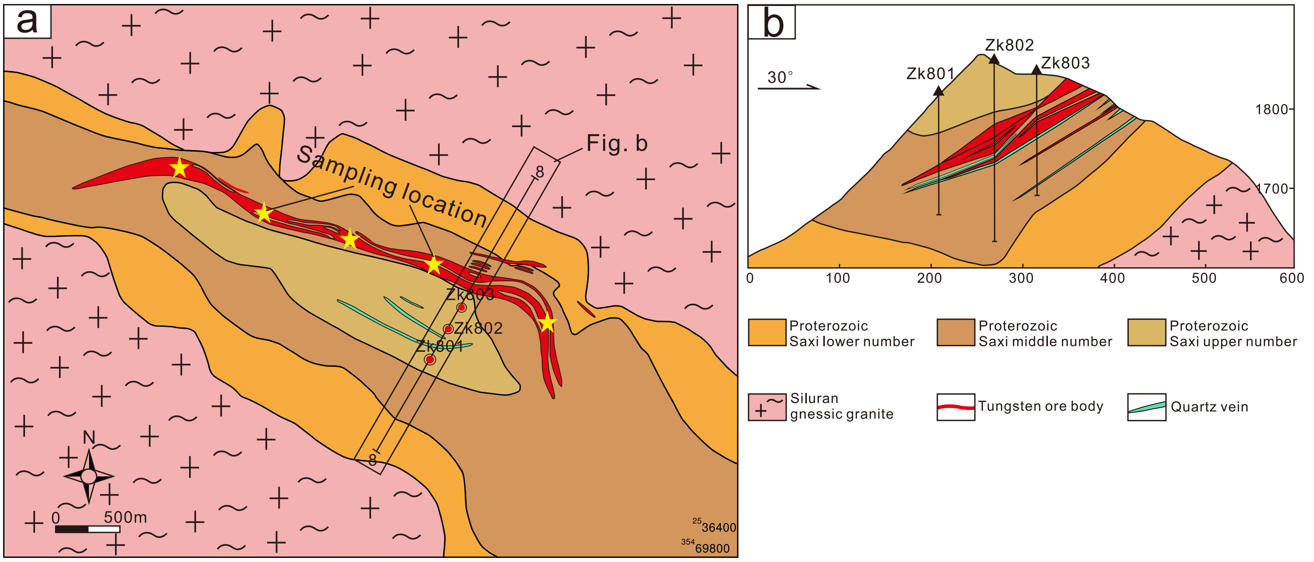

Fig. 2 **a** Geological sketch of the Saxi tungsten deposit; **b** geological profile of the No. 8 exploration line (modified from Wenshan Malipo Zijin Tungsten Industry Group Co. Ltd., Geological Exploration Department, 2009)

Nanyangtian Formation, composed of mica schist and metagreywacke. Stratiform ductile shear zones have developed within the Saxi Formation, exhibiting significant mylonitization and slicing. These shear zones host intense late-stage hydrothermal metasomatic mineralization, serving as ore-bearing structures that produce high-quality tungsten in the mining area (Long et al. 2021). Tungsten mineralization at Saxi primarily occurs within the middle number of the Proterozoic Saxi Formation and can be categorized into two types: stratiform and vein. Stratiform mineralization is predominantly hosted within the granulite, which is characterized by alternating dark and light bands, with scheelite distributed linearly along foliation planes and showing stable extensions, while vein mineralization is primarily associated with pegmatite dikes and quartz veins, which often crosscut or develop along the stratigraphy.

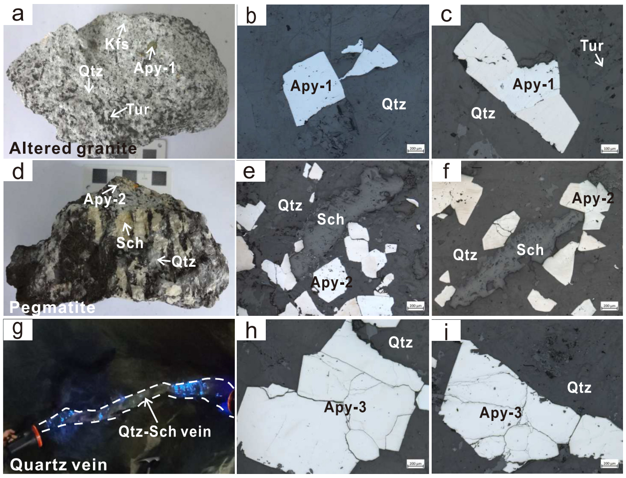

Fig. 3 Arsenoyrite from the Saxi deposit in rock samples and optical micrograph. Apy. arsenopyrite; Sch. scheelite; Qtz. quratz; Tur. tourmaline; Kfs. K-feldspar. **a** Photograph of the sample from altered granite. **b** Photograph of the Apy-1 and quartz symbiosis. **c** Photograph of the Apy-1, quartz and tourmaline. **d** Photograph of the sample from pegmatite dike tungsten. **e** Photograph of the scheelite and Apy-2 symbiosis. **f** Photograph of Apy-2 sample from pegmatitic vein-type tungsten orebody. **g** Photograph of the field fluorescence from sample from quartz vein-type tungsten orebody. **h** Photograph of the Apy-3 and quartz symbiosis. **i** Photograph of Apy-3 sample from quartz vein-type tungsten orebody

3 Occurrence of the arsenopyrite

Tungsten orebodies in the Saxi deposit occur in stratiform and vein forms. This research focuses on the vein-type orebodies. Through detailed investigations of ore textures, cross-cutting relationships and mineral assemblages, three generations of arsenopyrite hosted in vein-type mineralizations have been distinguished: (1) arsenopyrite within the altered granite, (2) arsenopyrite within the pegmatite dikes, and (3) arsenopyrite within the quartz veins (Fig. 3). Arsenopyrite within the altered granite (Apy-1) is euhedral and medium-grained and is associated with K-feldspar, plagioclase, quartz, tourmaline, biotite, apatite and scheelite (Fig. 3a–c). Arsenopyrite within the pegmatite dikes (Apy-2) is euhedral-subhedral and medium-grained and is associated with feldspar, quartz and scheelite (Fig. 3d–f). Arsenopyrite within the quartz veins (Apy-3) is anhedral and coarse-grained and is closely associated with quartz and scheelite (Fig. 3g–i). Three distinct paragenetic stages have been recorded in the study area and can be distinguished using ore textures, cross-cutting relationships and mineral assemblages, which record the change of the magmatic stage (stage I), transition stage of magmatic hydrothermal (stage II) and hydrothermal stage (stage III) (Fig. 4). This paper also summarizes the characteristics of different depths of rock types (Fig. 5). According to the occurrence and sampling location of arsenopyrite, we believe that the three generations of arsenopyrite are the products of evolution of tungsten-bearing granitic magmatic hydrothermal in different parts of the crust.

4 Sampling and analytical methods

The samples were taken from the middle number of Saxi Formation, including tungsten-altered granite, pegmatite dike and quartz vein ores, according to their occurrences. We chose apatite with relatively good preservation in the altered granite for U–Pb dating. We also selected arsenopyrites, which are closely related to scheelite in each stage for trace element and in situ S–Pb isotope analysis.

4.1 In situ apatite U–Pb dating

Apatite samples were collected from the drill core of altered granite at the Saxi deposit. Apatite U–Pb isotopic dating was conducted using LA-ICP-MS at the Guangzhou Tuoyan Analytical Technology Co. Ltd. (GTAT). The analysis employed a New Wave Research 193-nm ArF excimer laser ablation system in conjunction with a Thermo Scientific iCap-RQ quadrupole inductively coupled plasma mass spectrometer (ICP-MS). Specifications for the laser beam included a 50 μm spot diameter, 6 Hz frequency and 4.0 J/cm^2 energy density. The silicate glass reference materials NIST 610, BCR-2G (Jochum et al. 2011) and MAD (473.5±0.7 Ma; Chew et al. 2014) were utilized as external standards to correct for instrument mass discrimination. Each time-resolved analysis comprised approximately 45 s of blank signal followed by 40 s of sample signal. Two sets of standard sample tests were interspersed between every six unknown samples. Raw test data were processed offline using IOLITE software (Paton et al. 2011). Age calculations and concordant mapping were performed using Isoplot R (Vermeesch 2018).

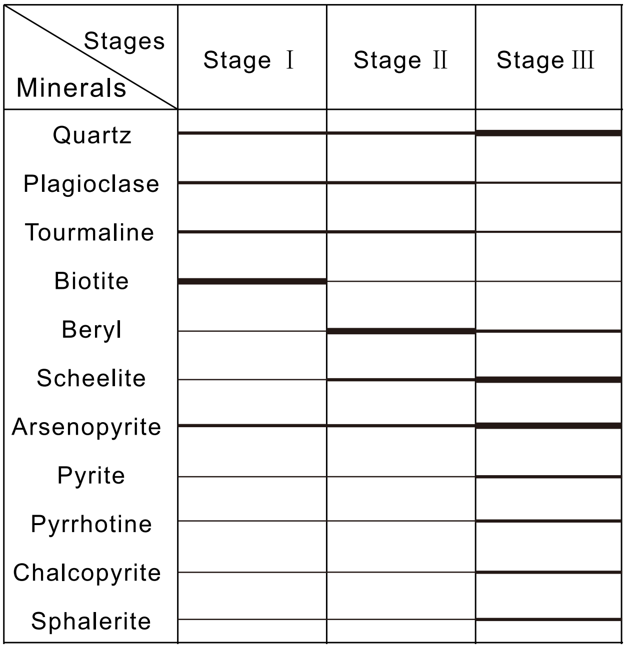

Fig. 4 Paragenetic sequence of minerals in the Saxi deposit. The thickness of line indicates the mineral amounts in the paragenetic sequence

4.2 In situ trace element analysis of arsenopyrite

The trace elements in arsenopyrite were analyzed using a New Wave Research (NWR) 193-nm ArF Excimer laser-ablation system coupled with an iCAP RQ ICP-MS at the GTAT. The ICP-MS was calibrated with NIST SRM 610 to minimize oxide production. The laser fluence was set to 3.5 J/cm^2, with a repetition rate of 6 Hz, a spot size of 30 μm and an analysis duration of 45 s, followed by a 40-s background measurement. The trace element concentrations in arsenopyrite were calibrated against several reference materials, including NIST SRM 610 and MASS-1 (Liu et al. 2008; Jochum et al. 2011). The sulfide pellet standards SRM 612 and GE8 were used as monitor samples to ensure data accuracy (Wilson et al. 2002; Danyushevsky et al. 2011). The analytical accuracy is > 20% for most elements. Offline processing of the analytical data was carried out using the 3D Trace Elements DRS mode of the IOLITE software (Paton et al. 2011).

4.3 In situ S isotopic analysis of arsenopyrite

A total of 22 arsenopyrite grains from the Saxi deposit were analyzed for S isotopes using a Thermo Scientific Neptune Plus Multi-Collector Inductively Coupled Plasma Mass Spectrometer (MC-ICP-MS), coupling with a New Wave Research 193-nm ArF laser ablation system. Faraday cups L3, C and H3 were assigned to detect ^{34}S, ^{33}S and ^{32}S, respectively. The laser energy density (fluence) was set to 3.5 J/cm^2, with a frequency of 3 Hz and spot size of 30 μm. Data acquisition was performed in TRA mode, with a 15-s background acquisition, a 40-s sample integration time and a 70-s purge time (Chen et al. 2017; Bao et al. 2017; Yuan et al. 2018). A matrix-matching standard WS1 ($\delta^{34}S_{V\text{-}CDT} = 1.1$, 2SE $= 0.2$) was used as the internal standard to evaluate the reliability of the unknown sample

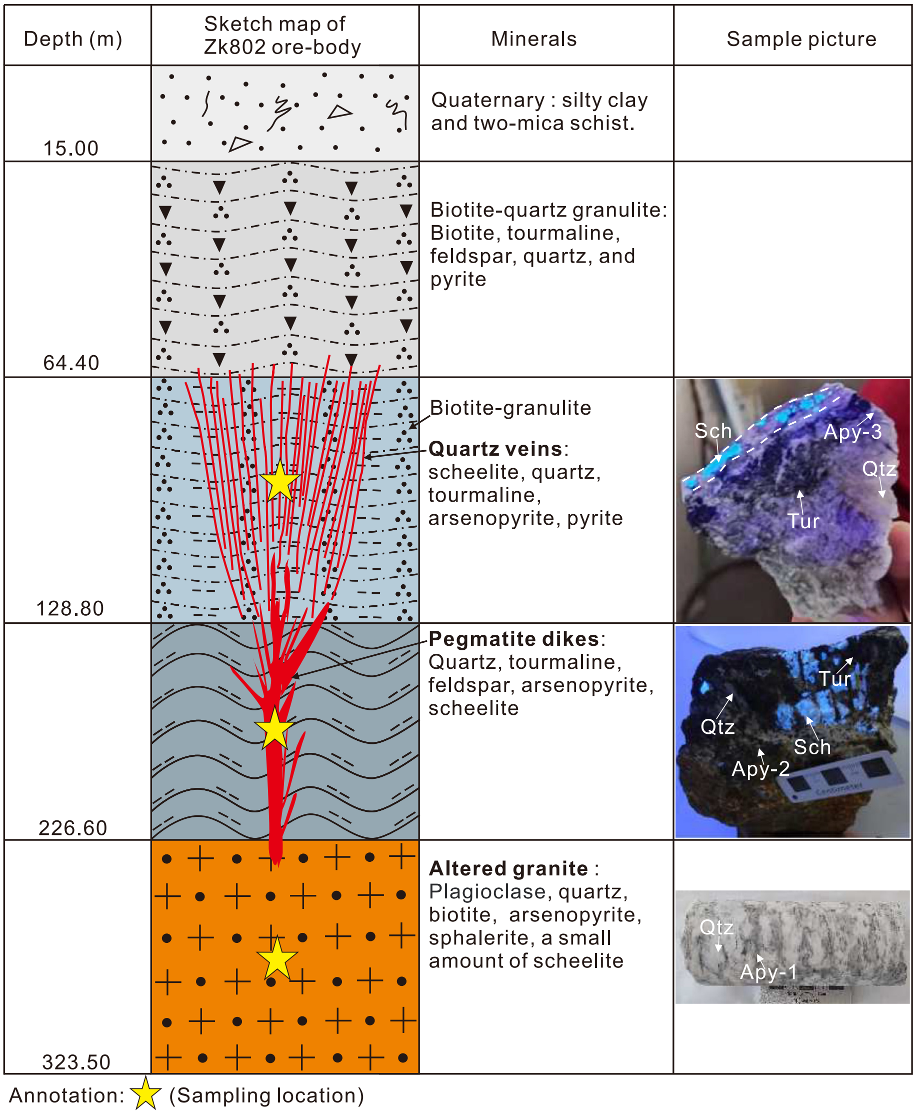

Fig. 5 Summary of the characteristics of different orebody depths and the distinct occurrences of the three generations of arsenopyrites. In sample pictures, abbreviations: Apy. arsenopyrite; Qtz. quartz; Sch. scheelite; Tur. tourmaline

Depth (m)	Sketch map of Zk802 ore-body	Minerals	Sample picture
15.00		Quaternary : silty clay and two-mica schist.	
64.40		Biotite-quartz granulite: Biotite, tourmaline, feldspar, quartz, and pyrite	
128.80		Biotite-granulite **Quartz veins**: scheelite, quartz, tourmaline, arsenopyrite, pyrite	
226.60		**Pegmatite dikes**: Quartz, tourmaline, feldspar, arsenopyrite, scheelite	
323.50		**Altered granite** : Plagioclase, quartz, biotite, arsenopyrite, sphalerite, a small amount of scheelite	

data. The $\delta^{34}S$ value for the monitoring sample, Balmat ($\delta^{34}S_{V\text{-}CDT=}16.3$, 2SE = 0.3), obtained during this analysis aligns with the recommended value within the error range; the analysis accuracy is better than ± 0.2%.

4.4 In situ Pb isotopic analysis of arsenopyrite

A total of 23 arsenopyrite grains from the Saxi deposit were analyzed for Pb isotopes using the LA-MC-ICP-MS at the GTAT. The LA employed a 193-nm excimer laser ablation system (RESOlution M-50, ASI), consisting of a 193-nm ArF excimer laser, a dual-chamber sample chamber and a computer-controlled high-precision X–Y sample positioning system. This dual-chamber design effectively prevents cross-contamination between samples, reduces sample purging time and enhances loading capacity, thereby minimizing the influence of human factors during frequent sample changes. The laser energy density was set to 6 J/cm^2, with a frequency of 5 Hz. The laser spot size ranged from 9 to 120 µm, depending on Pb content, and high-purity helium was used as the carrier gas at a flow rate of 280 ml/min. Pb isotopes were measured using the Nu Plasma II MC-ICP-MS, the latest generation dual-focus multi-collector plasma mass spectrometer from Nu Instruments (Bao et al. 2017; Yuan et al. 2018). Faraday cups H2, H1, Ax, L2 and L4 were designated to collect ^{208}Pb, ^{207}Pb, ^{206}Pb, ^{204}Pb+Hg and ^{202}Hg, respectively. Pb isotope mass fractionation was calibrated using the "standard-sample-standard-sample" cross-rule SSB. Simultaneously, ^{202}Hg and the ratio ^{202}Hg/^{204}Hg=0.229883 were measured to eliminate the interference of ^{204}Hg on ^{204}Pb, ensuring accurate signal values for ^{204}Pb. During analysis, the internal standard galena Gn01 and pyrite powder tablet PSPT-2 were used as monitoring samples, with an international standard sample inserted after every three unknown samples. Data acquisition was conducted in TRA mode, with a background acquisition time of 30 s, a sample integration time of 50 s and a purging time of 40 s.

5 Results

5.1 Apatite U–Pb age

Apatite U–Pb age data are presented in Table S1 and illustrated in Fig. 6. Fifteen LA-ICP-MS spot analyses conducted on sample SX22-39-1 yielded an age of 147.0±4.0 Ma (MSWD = 1.3) (Fig. 6).

5.2 Trace element compositions of arsenopyrite

A total of 32 LA-ICP-MS spot analyses were performed, consisting of 10 spots each on Apy-1 and Apy-2 and 12 spots on Apy-3. Each analysis consists of 3 major elements and 62 trace elements, with 12 exhibiting significant variations, including S, Fe, Co, Ni, As, Se, Ag, Sb, Te, W, Pb and Bi. The LA-ICP-MS element compositions of arsenopyrites are given in Table S2 and plotted in Figs. 7, 8 and 9.

Time-resolved measurements for each laser spot analysis were used to ascertain whether a specific trace element occurred within the arsenopyrite lattice as a substitution for major elements or as a nano-or micro-sized inclusion (Maslennikov et al. 2009a, b; Nie et al. 2021). In this study, most trace elements in arsenopyrite, such as V, Cr, Mn, Ga, Ge, Rb, Sr, Nb, Mo, Cd, Sn, Au, Hg, Os and Th, were below the detection limit. Time-resolved depth profiles for three types of arsenopyrite show that Fe, Co, Ni, Sb and As are also relatively smooth and consistent in their concentrations regarding Se and Te, indicating that these elements were rather homogeneous and were exchanged via substitution in arsenopyrite (Fig. 7a–c). However, there are notable compositional differences in their trace element content. Apy-2 is more enriched in Co, Ni, Se, Ag, Sb, Te, W, Pb and Bi than Apy-1 and Apy-3, with concentration differences spanning several orders of magnitude. The distribution map of trace elements indicates that the levels of Bi, Sb, Se, Te and W are lower in Apy-1 and Apy-3 than in Apy-2 (Fig. 8). Overall, the content of these trace elements increases from Apy-1 to Apy-2 before decreasing in Apy-3.

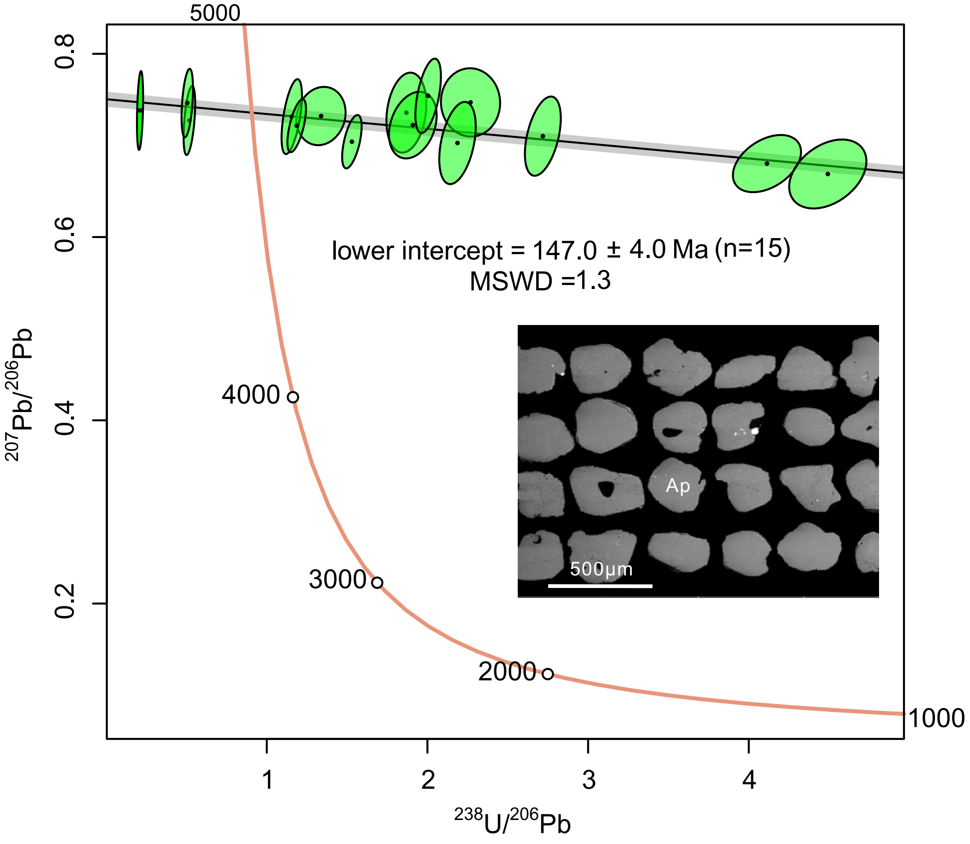

Fig. 6 LA-ICP-MS U–Pb Tera-Wasserburg concordia diagram of apatites and the BSE image of apatites in the altered granite from Saxi tungsten deposit

Fig. 7 LA-ICP-MS time-resolution depth profile of arsenopyrite data, showing distribution of elements in arsenopyrite from Saxi deposit. **a** Apy-1; **b** Apy-2; **c** Apy-3

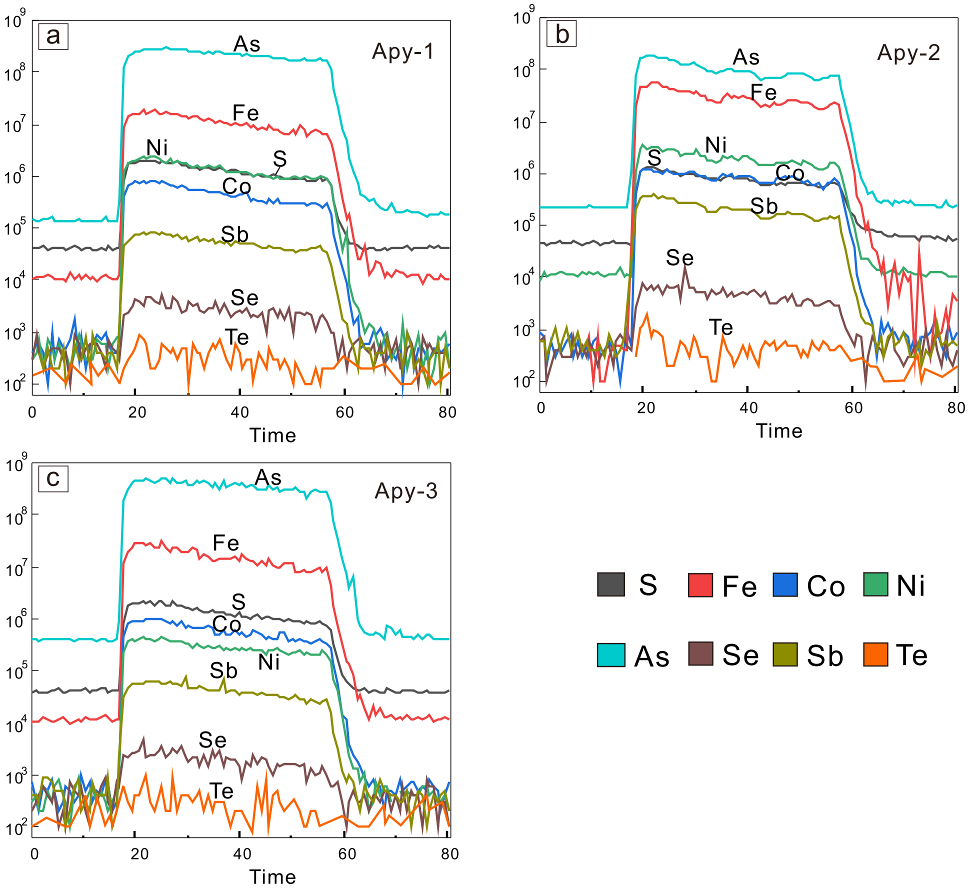

Fig. 8 Distribution of main trace elements in three kinds of arsenopyrite

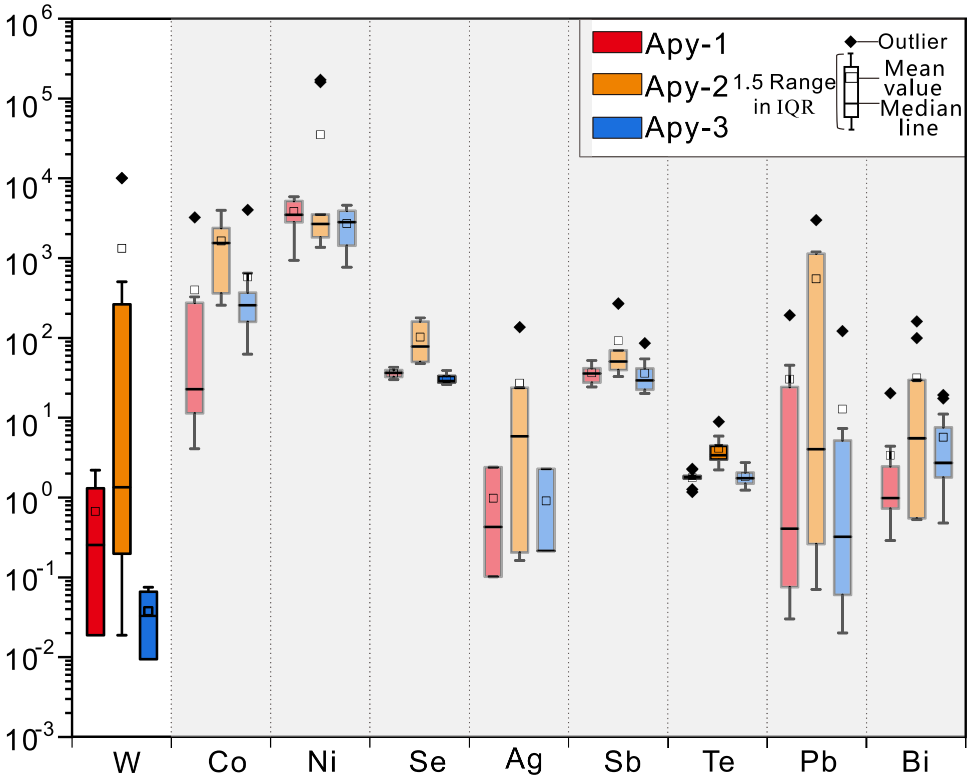

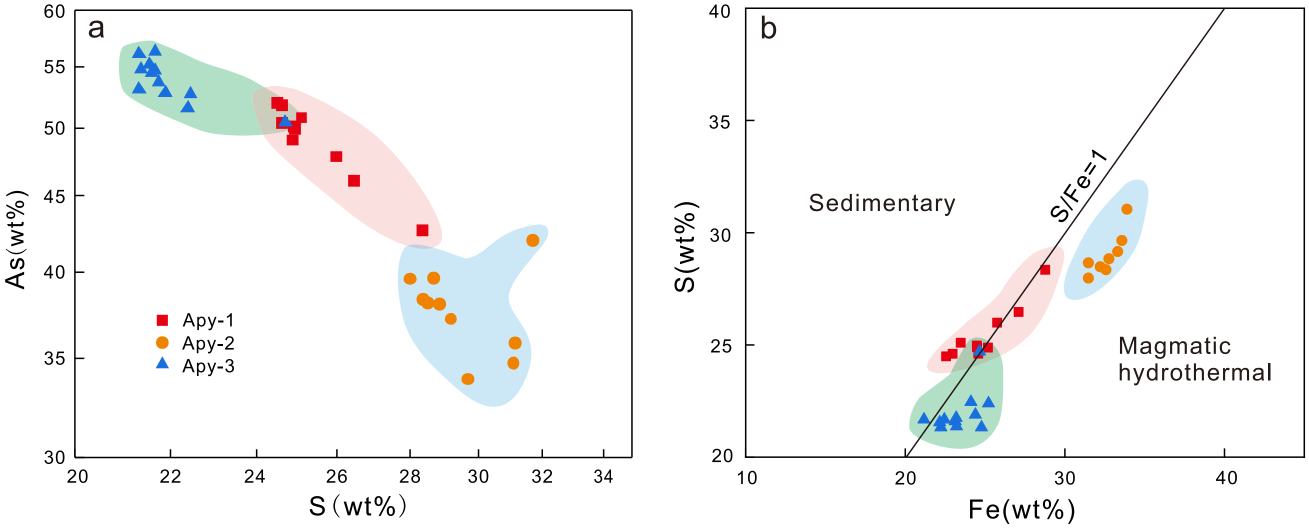

Fig. 9 Trace element plots of arsenopyrites in three stages from the Saxi tungsten deposit. See text for additional explanation. **a** As versus S; **b** S versus Fe

The LA-ICP-MS data reveal a general negative correlation between As and S concentrations in Apy-1, Apy-2 and Apy-3, with the As/S ratio highest in Apy-3 and lowest in Apy-2 (Fig. 9a). This inverse relationship between As and S in arsenopyrites suggests a coupled substitution process during formation (Lee et al. 2019). Conversely, the S/Fe ratio demonstrates a generally positive relationship across the three arsenopyrite types (Fig. 9b).

5.3 S–Pb isotopic compositions of arsenopyrite

A total of 22 sulfur isotopic analyses were conducted on samples Apy-1 to Apy-3, with results presented in Table S3 and plotted in Fig. 10. The δ^{34}S values range from 4.29‰ to 8.11‰. Specifically, five analyses were performed on arsenopyrite from both Apy-1 and Apy-2, while six analyses were conducted on arsenopyrite from Apy-3. The three generations of arsenopyrite exhibit broadly similar sulfur isotope values, with δ^{34}S ranges as follows: 4.31‰ to 6.66‰ for Apy-1, 4.76‰ to 8.11‰ for Apy-2 and 4.29‰ to 4.96‰ for Apy-3, yielding mean values of 5.26‰, 6.07‰ and 4.74‰, respectively. These sulfur isotopic data indicate that δ^{34}S values within individual arsenopyrite grains are relatively consistent (Table S3).

In-situ Pb isotope results for arsenopyrite from ten tungsten ore samples are presented in Table S4 and plotted in Fig. 11. For Apy-1, the Pb isotope ratios are as follows: ^{206}Pb/^{204}Pb ranges from 18.292 to 20.632, ^{207}Pb/^{204}Pb ranges

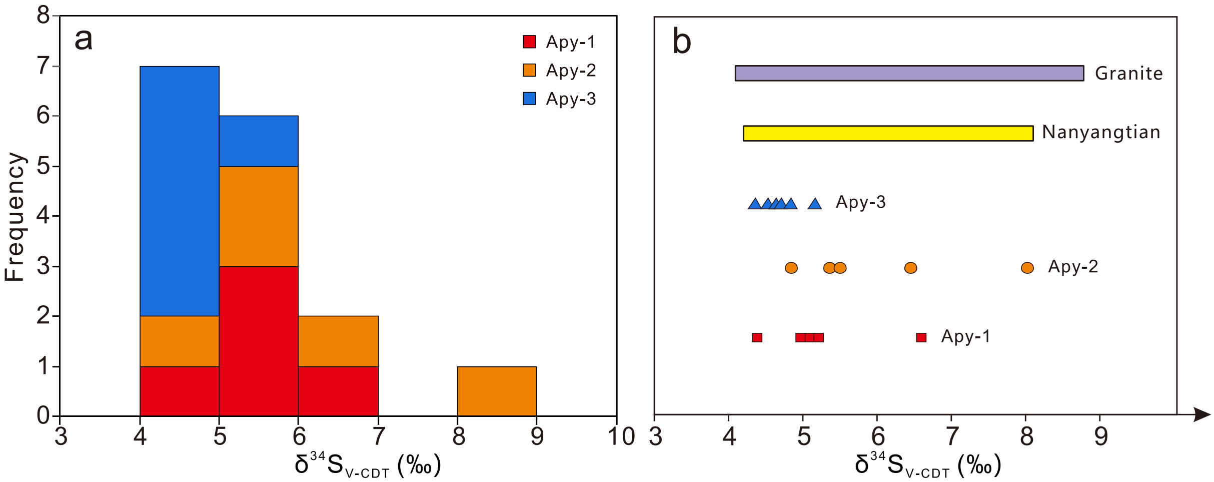

Fig. 10 **a** In situ sulfur isotope composition histogram of arsenopyrite of different mineralization stages. **b** Comparison of isotopic values of arsenopyrite in different stages and the pyrite from Nanyngtian

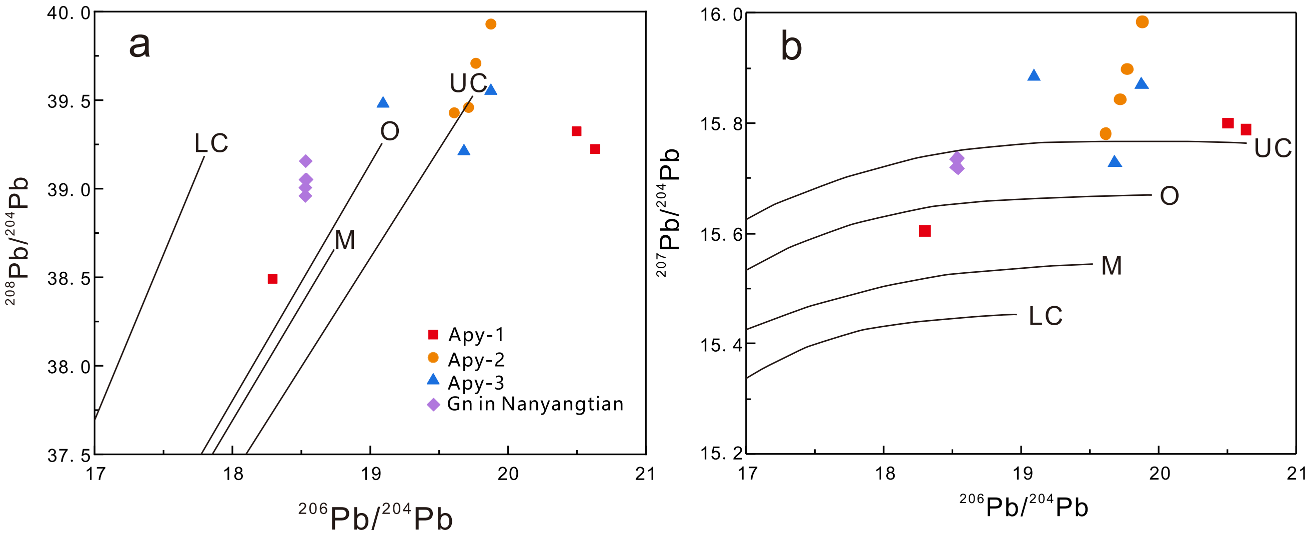

Fig. 11 Pb isotopic composition of samples from the Saxi deposit plotted with the evolution curve of Zartman and Doe (1981); **a** ^{208}Pb/^{204}Pb versus ^{206}Pb/^{204}Pb; **b** ^{207}Pb/^{204}Pb vs. ^{206}Pb/^{204}Pb; UC. upper crust; O. orogen; M. mantle; LC. lower crust

from 15.605 to 15.801 and ^{208}Pb/^{204}Pb ranges from 38.491 to 39.224. In Apy2, the values are 19.610 to 19.876 for ^{206}Pb/^{204}Pb, 15.782 to 15.985 for ^{207}Pb/^{204}Pb and 39.428 to 39.929 for ^{208}Pb/^{204}Pb. For Apy3, the Pb isotope ratios range from 19.093 to 19.875 for ^{206}Pb/^{204}Pb, 15.729 to 15.885 for ^{207}Pb/^{204}Pb and 39.211 to 39.552 for ^{208}Pb/^{204}Pb.

6 Discussion

6.1 Origin of arsenopyrite

The origin of sulfides exhibits considerable diversity, encompassing primarily sedimentary and magmatic-hydrothermal sources (Bralia et al. 1979; Cook et al. 2009; Chen et al. 2020; Li et al. 2020). In this study, we attribute a magmatic-hydrothermal origin to the arsenopyrite, supported by several lines of evidence.

The occurrence of these three arsenopyrite types reveals distinct characteristics. Apy-1, found within altered granite, is closely associated with feldspar and quartz (Fig. 3a–c), aligning more closely with a magmatic-hydrothermal origin. Apy-2 and Apy-3 occur within pegmatitic dike and quartz vein orebodies, respectively, and are associated with scheelite (Fig. 3d–i), which also supports a magmatic-hydrothermal origin.

The age data provide additional insights into the origin of arsenopyrite (Fig. 5). The apatite, associated with Apy-1, in W-bearing altered granite appears homogeneous under the backscattered electron (BSE) images (Fig. 5b), indicating it has not been altered by hydrothermal metasomatism, thus allowing its age to represent the magmatic event of this period. The U–Pb age of the apatite is determined to be 147.0±4.0 Ma (Fig. 5a), which does not correspond to any known magmatic events in the studying area. Notably, scheelite in the quartz vein from the Nanyangtian W deposit shows similar ages (146–141 Ma, Zhao et al. 2024) and is proposed to originate from concealed granite. Given the proximity of Nanyangtian to the Saxi deposit, it is plausible that vein-type tungsten in the Saxi deposit also originated from a concealed granitic intrusion around 147 Ma. In addition, the U–Pb age of vein scheelite obtained by the our team is 150.6±4.0 Ma , which further indicates that vein-type scheelite mineralization is related to Early Cretaceous magmatic hydrothermal system.

The S/Fe ratios in these three arsenopyrite types suggest that the fluids may have originated from a magmatic-hydrothermal source (Fig. 9b). Generally, hydrothermal arsenopyrite is sulfur-deficient, whereas sedimentary arsenopyrite is either enriched in sulfur or close to the ideal arsenopyrite composition (S/Fe=1) (Brill 1989; Li et al. 2020). In the Saxi deposit, the S/Fe ratios for Apy-1, Apy-2 and Apy-3 range from 0.98 to 1.09, 0.89 to 0.92 and 0.86 to 1.02, respectively (average 0.97 < 1, Table S2). Consequently, the primary source of sulfide sulfur in the Saxi deposit is likely deep-seated or magmatic.

The sulfur isotope compositions provide additional evidence for the origin of arsenopyrite (Fig. 10). Sulfur isotopic ratios serve as a well-established tracer, particularly useful for identifying ore deposit genesis (Ohmoto 1972). Previous studies have identified four primary sources of sulfur in ore deposits: deep sulfur or magmatic sulfur (δ^{34}S ≈ 0), crustal sulfur, seawater sulfur and mixed sulfur sources. The δ^{34}S values for the three arsenopyrite types in the Saxi tungsten deposit range from 4.29‰ to 8.11‰ (Table S3), suggesting a deep magmatic sulfur source, consistent with ore-forming fluids of magmatic-hydrothermal origin. Although the specific sulfur source for the Saxi tungsten deposit cannot be conclusively identified based solely on the δ^{34}S compositions of arsenopyrite, the δ^{34}S values of pyrites from the nearby Nanyangtian W deposit display similar characteristics (4.2‰ to 8.1‰, and 7.46‰ to 9.55‰; Feng et al. 2011b; Zhang et al. 2021). This similarity provides a reference for understanding the sulfur source in the Saxi deposit, as these δ^{34}S values align with those of granitic sulfur, suggesting a common sulfur reservoir. Together, these values support a deep or magmatic sulfur source, reinforcing the interpretation of a magmatic-hydrothermal origin for these deposits. In addition, the δ^{34}S value of pyrites in the Zhuxi skarn W-Cu deposit is 2.4‰ to 4.0‰ (Pan et al. 2020), and the vein-hosted sulfides have δ^{34}S values of 3.8‰–6.3‰ in the Shizhuyuan W deposit (Wu et al. 2018), which further indicates that ore-forming fluid of the Saxi deposit is similar to these tungsten deposits in South China, and they are related to granitic magmatic hydrothermal.

The Pb isotopic compositions of the three generations of arsenopyrite in the Saxi deposit suggest that ore-forming materials were sourced primarily from the upper crust (Fig. 10). Lead isotopes exhibit minimal fractionation during physical and chemical processes, except through radioactive decay, which allows them to remain relatively stable during the migration and precipitation of ore-forming materials. Consequently, Pb isotopes and related parameters are widely used to trace the sources of ore-forming materials in metal deposits (Zartman and Doe 1981; Mirnejad et al. 2011). Table S4 presents the in situ Pb isotope compositions of sulfides from the three ore types in Saxi, alongside comparative Pb isotopic data from the Nanyangtian tungsten deposit in the Laojunshan ore district (Feng et al. 2011). The generally similar lead isotopic compositions among tungsten deposits in this region suggest common source characteristics. In the Zartman's lead tectonic evolution diagram, Pb isotopic signatures from surrounding rock lead in the Laojunshan ore concentration area are scattered and mostly distinct from those of ore lead, indicating minimal influence from surrounding rock on ore lead and suggesting these surrounding rocks are not the primary source. Notably, some samples project near the lower crust and orogenic zone, reflecting inheritance from deeper early-stage lead sources. In contrast, other samples from the Saxi deposit, along with those from Nanyangtian, plot above or near the upper crustal evolution line, indicating superposition from later-stage metamorphic or granitic hydrothermal sources. Additionally, most Pb isotopic compositions of the chalcopyrite, pyrite and sphalerite of Zhuxi deposit in Jiangxi Province were also plotted in the field between the upper crust and orogen (Pan et al. 2020), reflecting that their ore-forming material sources are similar, originating from the upper crust.

6.2 Ore-forming fluid evolution and insight for W mineralization

The content and ratios of trace elements in arsenopyrite contain valuable genetic information, making it an effective tool for determining the genetic type of ores, assessing the source of ore-forming materials and tracing the evolution of ore-forming fluids (Reich et al. 2005; Cook et al. 2013). The migration mechanisms of trace elements among the three types of arsenopyrite are complex, influenced by factors such as temperature during the evolution of the ore-forming fluids (Cook et al. 2013; Reich et al. 2013; Gregory et al. 2016). Therefore, microanalysis and elemental compositions of arsenopyrite offer crucial insights into the chemical variations of hydrothermal fluids during the continuous growth of sulfide minerals.

The As/S ratio reflects temperature variation during fluid evolution (Fig. 9a). The As/S ratio is particularly sensitive to temperature in sulfur-buffered assemblages, with higher ratios observed at higher temperatures (Kretschmar and Scott 1976; Koh et al. 1992; Lentz 2002). Apy-1 in altered granite is characterized by higher As/S ratios than Apy-2 in pegmatite dike orebodies, indicating a decrease in temperature from Apy-1 to Apy-2. In contrast, the As/S ratio of Apy-3 in quartz vein orebodies is higher than that of Apy-1 and Apy-2, likely because of the intensive interaction between the hydrothermal fluid and the surrounding rocks, which extracts As from the surrounding materials, resulting in higher As content in Apy-3. This suggests that these arsenopyrites may have formed at medium to high temperatures, which is consistent with the homogenization temperature of fluid inclusions in quartz vein-type orebodies (165–340 °C, Zhang et al. 2016). Furthermore, variations in δ^{34}S value among the three arsenopyrite types provide information on fluid evolution (Fig. 10). From Apy-1 to Apy-3, the sulfur isotope values increase initially and then decrease, which may reflect a stage during the magmatic-hydrothermal transition when temperatures decrease, sulfur-bearing gases volatilize and heavy sulfur minerals are left behind. During the hydrothermal stage, fluid interaction with surrounding rocks leads to the consumption of sulfur, consistent with the observed As/S ratio trends in the three arsenopyrite generations.

The trace element box pattern provides valuable insights into W mineralization (Fig. 8). The W content initially increases and then decreases from Apy-1 to Apy-3. We propose that in the magmatic and magmatic-hydrothermal transitional stages, W primarily existed as a solid solution within the arsenopyrite lattice. As the temperature gradually decreased, part of scheelite in the pegmatite dikes began to precipitate. During the hydrothermal stage, metasomatic reactions between the fluid and surrounding rocks occurred, where Ca from the surrounding rocks combined with W in the fluid, leading to the precipitation of significant amounts of scheelite in the quartz veins. This process resulted in a decrease in W content in Apy-3.

In summary, these results suggest that the hydrothermal fluids responsible for W mineralization enriched As while depleting sulfur in the arsenopyrite grains found in quartz veins. This also indicates that the vein-type tungsten mineralization in the Saxi deposit underwent a magmatic to hydrothermal evolution, with mineralization beginning during the magmatic-hydrothermal transitional stage, followed by significant mineralization during the hydrothermal stage. This is consistent with the presence of both melt inclusions and gas-liquid inclusions in the tungsten-bearing quartz veins as well as with the H–O isotope data from quartz (Sheng 2016; Sheng et al. 2023), indicating that the primary fluid source is magmatic water, with contributions from organic or meteoric water.

6.3 A model for vein-type tungsten mineralization

Systematic investigations of the vein-type tungsten occurrences, apatite U–Pb age in W-bearing altered granite and trace element and S–Pb isotopic compositions of arsenopyrite in the Saxi deposit have led to the proposal of a model for vein-type tungsten mineralization (Fig. 12). The comprehensive studies of arsenopyrite suggest that the mineralization process occurred in the three stages.

The first stage, indicated by the apatite U–Pb age of 147.0 ± 4.0 Ma, is consistent with the vein-type scheelite U–Pb age 150.6 ± 4.0 Ma obtained by our team, suggesting that during the Early Cretaceous, a granitic magmatic episode occurred, potentially linked to the distant subduction of the Paleo-Pacific Plate (Fang et al. 2021; Sun et al. 2021; Zhao et al. 2024). Lithospheric extension caused crustal thinning and upper crust remelting, forming a deep, concealed granitic pluton. This process released W-rich magmatic-hydrothermal fluids through crystallization differentiation (Que et al. 2014; Cheng et al. 2016; Soloviev et al. 2017). At the deuteric stage, W-rich fluids, generated by the devolatilization within the W-bearing granitic magma chamber, migrated upward and potentially reacted with the granite at the chamber's margins to form the W-bearing altered granite (Peters 1987; Kajdas et al. 2017).

The second stage was primarily driven by the exsolution of ore-forming fluids, during which the numerous volatile components significantly reduced the viscosity of the residual melts, enhancing its fluidity, resulting in an increase in the content of W in Apy-2. The decrease of As/S ratio and increase of S isotope value in Apy-2 indicate that the decrease of temperature and the volatilization of sulfur-containing gas may be the mechanism of scheelite precipitation in pegmatite dikes (Sirbescu et al. 2003; Duke et al. 1990, 1992).

The third stage was influenced by the SE–NW thrust nappe structure, which created foliation and fissures within the Saxi Formation (Que et al. 2014; Bi et al. 2015), providing pathways and storage space for fluid migration and W mineralization. The increase in the As/S ratios and the decrease in δ^{34}S values in Apy-3 indicate that wallrock-derived fluids were introduced during this process, resulting in higher As content and lower S content in the formed

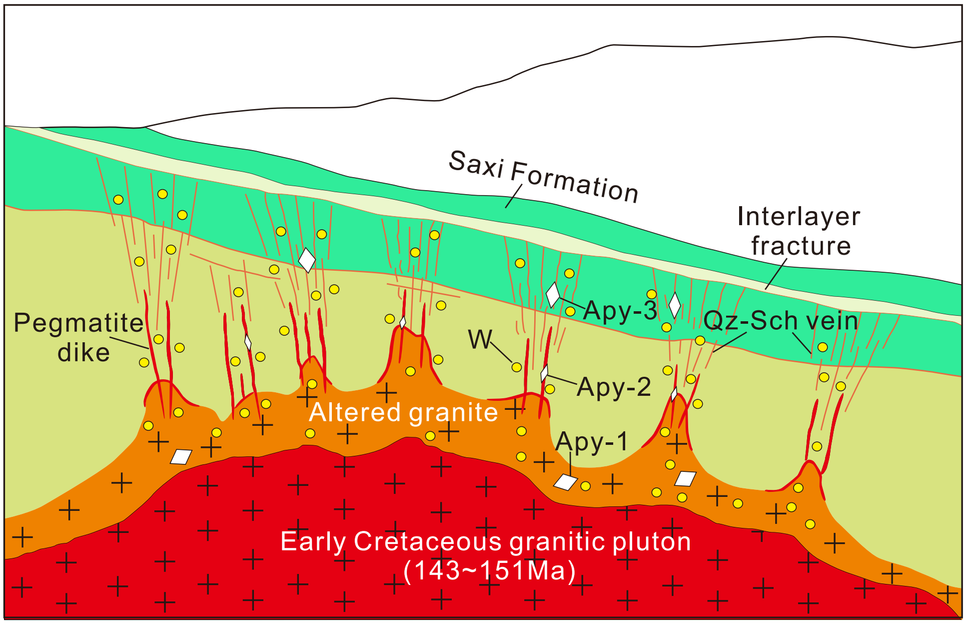

Fig. 12 Metallogenic models of vein-type tungsten in Saxi deposit

arsenopyrite formed. Water-rock reactions occurred between the mixed fluids and the interlayer carbonates, leading to the formation of quartz vein scheelite bodies, which were superimposed on schistosity planes.

These findings further support the hypothesis that the genesis of vein-type tungsten is closely associated with magmatic activity during Early Cretaceous.

6.4 Implication for the Saxi vein-type W mineralization

A statistical analysis of the typical quartz vein-type tungsten and skarn-type tungsten deposits in South China is shown in Table S5.

The Saxi deposit is a quartz-vein-type W–Be deposit, and no skarn is found in the ore area, which is different from some tungsten deposits in South China, such as Nanyangtian, Yaogangxian and Shizhuyuan, where both large-scale quartz-vein-type and skarn-type tungsten mineralization are present (Cai et al. 2018; Zhao et al. 2024; Ni et al. 2023), but according to the comparative analysis of their metallogenic models (Ni et al. 2023), their genesis is similar to Saxi, which is closely related to granite intrusion. Therefore, undiscovered granite and skarn-type tungsten mineralization may be the focus of further prospecting work in this area.

In terms of metallogenic temperature and age, the Saxi deposit is closely similar to other deposits in South China. Their metallogenic temperature ranges from 150 to 372 °C and indicates that the decrease of fluid temperature may be the mechanism of scheelite precipitation in this area. Notably, W-Sn mineralization in South China concentrated within 170–140 Ma, belonging to Late Jurassic to Early Cretaceous, corresponding to significant distant subduction of the paleo-Pacific plate (Fang et al. 2021; Sun et al. 2021). If the geological event around 147 Ma is confirmed as the principal period of the Saxi vein-type W mineralization, it will have a profound impact on the exploration strategies in the Laojunshan area. Consequently, targeting deep-buried granitic rock from the Late Jurassic-Early Cretaceous may represent a critical breakthrough in tungsten exploration within this region.

7 Conclusions

The vein-type tungsten of the Saxi deposit in southeastern Yunnan province is of deuteric origin interpreted based on in situ U–Pb dating of the apatite in altered granite, trace element analysis and S–Pb isotope studies of the three types of arsenopyrite. The following three conclusions are obtained below.

1. The apatite U–Pb age of 147.0±4.0 Ma provides evidence that tungsten mineralization in the Saxi deposit is likely associated with an Early Cretaceous concealed magmatic-hydrothermal system at depth.
2. Trace element analysis, along with sulfur and lead isotope studies of arsenopyrite, suggests that tungsten mineralization in the Saxi deposit formed under medium to high temperatures. The sulfur is inferred to have originated from a deep magmatic source, while the the granitic parental magma is derived from the upper crust.
3. A mineralization model for the vein-type tungsten in the Saxi deposit is proposed, with the findings supporting the conclusion that magmatic-hydrothermal processes were the primary mechanism driving the formation of vein-type tungsten in this region.

Acknowledgements This research was supported by funds from the Yunnan Major Scientific and Technological Project (grant No. 202202AG050006), National Natural Science Foundation project (grant No. 42272078) and the Yunnan Fundamental Research Project (grant no. 202401CF070094). We are grateful to Malipo Jinwei Mineral Co. Ltd., for its help during the field work. We also extend our appreciation to Yu-Bo Yang and Xiang-Yang Yin for help during LA-(MC)-ICP-MS analyses.

Author contributions Wanbo Li: data curation, formal analysis, investigation, software, writing—original draft, writing—review & editing; Mingguo Deng: funding acquisition, project administration, writing—review & editing; Qiang Weng: conceptualization, project administration, writing—review & editing; Wenchang Li: funding acquisition, project administration, methodology; Zhen Jia: writing—review & editing; Wenbo Song: software, investigation; Zhengrong Li: investigation; Jiafei Yang: investigation.

Funding Yunnan Major Scientific and Technological Project (grant no. 202202AG050006). National Natural Science Foundation project (grant No. 42272078). (3) Yunnan Fundamental Research Project (grant No. 202401CF070094).

Declarations

Conflict of interest The authors declare that they have no known competing financial interests or personal relationships that could have appeared to influence the work reported in this paper.

References

Bao ZA, Chen L, Zong CL, Yuan HL, Chen KY, Dai MN (2017) Development of pressed sulfide powder tablets for in situ sulfur and lead isotope measurement using LA-MC-ICP-MS. Int J Mass Spectrom 421:255–262. https://doi.org/10.1016/j.ijms.2017.07.015

Bi MF, Zhang D, Wu GG, Di YJ, Que CY, Pan JB, Xue W (2015) Mesozoic tectonic deformation and ore-controlling of tungsten polymetallic deposits in Malipo area, southeastern Yunnan. Earth Sci Front 22(4):223–238 (**in Chinese with English abstract**). https://doi.org/10.13745/j.esf.2015.04.023

Bralia A, Sabatini G, Troja F (1979) A revaluation of the Co/Ni ratio in pyrite as geochemical tool in ore genesis problems: evidences from southern Tuscany pyritic deposits. Miner Deposita 14(3):353–374. https://doi.org/10.1007/BF00206365

Brill BA (1989) Trace-element contents and partitioning of elements in ore minerals from the CSA Cu–Pb–Zn deposit, Australia, and implications for ore genesis. Can Miner 27(2):263–274

Cai QR, Yan YF, Yang GS, Jia FJ, Li C (2018) Genesis of the Nanyangtian scheelite deposit in southeastern Yunnan Province, China: evidence from mineral chemistry, fluid inclusions, and C-O isotopes. Acta Geochim 37(4):614–631. https://doi.org/10.1007/s11631-017-0257-0

Chai FM, Zhang ZC, Wang W, Xie QH, Huang H, Zhang Y, Qi DM, Zhang XB (2023) New insights into the multiple magmatic fluid generations from scheelite in the Bastielieke W-polymetallic deposit, Chinese Altay (NW, China). Geosci Front 14(3):101532. https://doi.org/10.1016/j.gsf.2022.101532

Chen L, Chen KY, Bao ZA, Liang P, Sun TT, Yuan HL (2017) Preparation of standards for in situ sulfur isotope measurement in sulfides using femtosecond laser ablation MC-ICP-MS. J Anal at Spectrom 32(1):107–116. https://doi.org/10.1039/C6JA00270F

Chen LL, Ni P, Li WS, Ding JY, Pan JY, Wang GG, Yang YL (2018) The link between fluid evolution and vertical zonation at the Maoping tungsten deposit, Southern Jiangxi, China: fluid inclusion and stable isotope evidence. J Geochem Explor 192:18–32. https://doi.org/10.1016/j.gexplo.2018.01.001

Chen FC, Deng J, Wang QF, Huizenga JM, Li GJ, Gu YW (2020) LA-ICP-MS trace element analysis of magnetite and pyrite from the Hetaoping Fe–Zn–Pb skarn deposit in Baoshan block, SW China: implications for ore-forming processes. Ore Geol Rev 117:103309. https://doi.org/10.1016/j.oregeorev.2020.103309

Cheng YB, Mao JW, Liu P (2016) Geodynamic setting of late cretaceous Sn–W mineralization in southeastern Yunnan and northeastern Vietnam. Solid Earth Sci 1(3):79–88. https://doi.org/10.1016/j.sesci.2016.12.001

Chew DM, Petrus JA, Kamber BS (2014) U–Pb LA–ICPMS dating using accessory mineral standards with variable common Pb. Chem Geol 363:185–199. https://doi.org/10.1016/j.chemgeo.2013.11.006

Cook NJ, Chryssoulis SL (1990) Concentrations of invisible Au in the common sulfides. Can Miner 28:1–16

Cook NJ, Ciobanu CL, Mao JW (2009) Textural control on gold distribution in As-free pyrite from the Dongping, Huangtuliang and Hougou gold deposits, North China Craton (Hebei Province, China). Chem Geol 264(1–4):101–121. https://doi.org/10.1016/j.chemgeo.2009.02.020

Cook NJ, Ciobanu CL, Meria D, Silcock D, Wade B (2013) Arsenopyrite-pyrite association in an orogenic gold ore: tracing mineralization history from textures and trace elements. Econ Geol 108(6):1273–1283. https://doi.org/10.2113/econgeo.108.6.1273

Cui JM, Ni P, Peng ZQ, Pan JY, Li WS, Ding JY, Dai BZ, Gao Y, Han L, Zeng Q, Zhang T (2023) Tungsten mineralization formed by single-pulsed magmatic fluid: evidence from wolframite-hosted fluid inclusion from the giant Dajishan “five floor” style W-polymetallic deposit. Ore Geol Rev 157:105472. https://doi.org/10.1016/j.oregeorev.2023.105472

Danyushevsky L, Robinson P, Gilbert S, Norman M, Large R, McGoldrick P, Shelley M (2011) Routine quantitative multi-element analysis of sulphide minerals by laser ablation ICP-MS: standard development and consideration of matrix effects. Geochem Explor Environ Anal 11(1):51–60. https://doi.org/10.1144/1467-7873/09-244

Deditius AP, Utsunomiya S, Renock D, Ewing RC, Ramana CV, Becker U, Kesler SE (2008) A proposed new type of arsenian pyrite: composition, nanostructure and geological significance. Geochim Cosmochim Acta 72(12):2919–2933. https://doi.org/10.1016/j.gca.2008.03.014

Duke EF, Papike JJ, Laul JC (1992) Geochemistry of a boron-rich peraluminous granite pluton; the Calamity Peak layered granite-pegmatite complex, Black Hills, South Dakota. Can Miner 30(3):811–833

Duke EF, Shearer CK, Redden JA, Papike JJ, Lewry JF, Stauffer MR (1990) Proterozoic granite-pegmatite magmatism, Black Hills, South Dakota: structure and geochemical zonation. In: The Early Proterozoic Trans-Hudson Orogen of North America, vol 37. Geol Assoc Can, pp 253–269

Elongo V, Lecumberri-Sanchez P, Legros H, Falck H, Adlakha E, Roy-Garand A (2020) Paragenetic constraints on the Cantung, Mactung and Lened tungsten skarn deposits, Canada: implications for grade distribution. Ore Geol Rev 125:103677. https://doi.org/10.1016/j.oregeorev.2020.103677

Fang W, Dai LQ, Zheng YF, Zhao ZF, Ma LT, Zhao K (2021) Identification of Jurassic mafic arc magmatism in the eastern North China Craton: geochemical evidence for westward subduction of the Paleo-Pacific slab. Geol Soc Am Bull 133(7–8):1404–1420. https://doi.org/10.1130/B35787.1

Feng JR, Mao JW, Pei RF, Zhou ZH, Yang ZX (2010) SHRIMP zircon U–Pb dating and geochemical characteristics of Laojunshan granite intrusion from the Wazha tungsten deposit, Yunnan Province and their implications for petrogenesis. Acta Petrol Sin 26(3):845–857 (**in Chinese with English abstract**).

Feng JR, Mao JW, Pei RF, Li C (2011a) A tentative discussion on Indosinian ore-forming events in Laojunshan area of southeastern Yunnan: a case study of Xinzhai tin deposit and Nanyangtian tungsten deposit. Miner Depos 30(1):57–73. https://doi.org/10.16111/j.0258-7106.2011.01.010. (**in Chinese with English abstract**)

Feng JR, Mao JW, Pei RF, Li C (2011b) Ore-forming fluids and metallogenesis of Nanyangtian tungsten deposit in Laojunshan, southeastern Yunnan Province. Miner Depos 30(3):403–419. https://doi.org/10.16111/j.0258-7106.2011.03.003. (**in Chinese with English abstract**)

Feng JR (2011c) Ore-forming fluid characteristics and metallogenesis of tungsten deposit in Nanyangtian, Malipo, Yunnan Province (Ph.D. Dissertation). Chinese Academy of Geological Sciences, Beijing (**in Chinese with English abstract**)

Fleet M, MacLean P, Barbier J (1989) Oscillatory-zoned As-bearing pyrite from strata-bound and stratiform gold deposits. Econ Geol 6:356–362. https://doi.org/10.5382/Mono.06.27

Gregory DD, Large RR, Bath AB, Steadman JA, Wu S, Danyushevsky L, Bull SW, Holden P, Ireland TR (2016) Trace element content of pyrite from the Kapai Slate, St. Ives Gold District, western Australia. Econ Geol 111(6):1297–1320. https://doi.org/10.2113/econgeo.111.6.1297

Guo LG, Liu YP, Li CY, Xu W, Ye L (2009) SHRIMP zircon U–Pb geochronology and lithogeochemistry of Caledonian Granites from the Laojunshan area, southeastern Yunnan province, China: implications for the collision between the Yangtze and Cathaysia blocks. Geochem J 43(2):101–122. https://doi.org/10.2343/geochemj.1.0012

Hu RZ, Wei WF, Bi XW, Peng JT, Qi YQ, Wu LY, Chen YW (2012) Molybdenite Re–Os and muscovite ^{40}Ar/^{39}Ar dating of the Xihuashan tungsten deposit, central Nanling district, South China. Lithos 150:111–118. https://doi.org/10.1016/j.lithos.2012.05.015

Hua RM, Li GL, Zhang WL, Hu DQ, Chen PR, Chen WF, Wang XD (2010) A tentative discussion on differences between large-scale tungsten and tin mineralizations in South China. Miner Depos 29(1):9–23. https://doi.org/10.16111/j.0258-7106.2010.01.005. (**in Chinese with English abstract**)

Jiang GH, Hu RZ, Xie GQ, Zhao JH, Tang QL (2004) K-Ar ages of plutonism and mineralization at the dajishan tungsten deposit, Jiangxi province. China. Acta Mineral Sin 24(3):253–256.

https://doi.org/10.16461/j.cnki.1000-4734.2004.03.007. (**in Chinese with English abstract**)

Jochum KP, Weis U, Stoll B, Kuzmin D, Yang QC, Raczek I, Jacob DE, Stracke A, Birbaum K, Frick DA, Günther D, Enzweiler J (2011) Determination of reference values for NIST SRM 610–617 glasses following ISO guidelines. Geostandard Geoanalyt Res 35(4):397–429. https://doi.org/10.1111/j.1751-908x.2011.00120.x

Kajdas B, Michalik MJ, Migoń P (2017) Mechanisms of granite alteration into grus, Karkonosze granite, SW Poland. CATENA 150:230–245. https://doi.org/10.1016/j.catena.2016.11.026

Koh YK, Choi SG, So CS, Choi SH, Uchida E (1992) Application of arsenopyrite geothermometry and sphalerite geobarometry to the Taebaek Pb–Zn (–Ag) deposit at Yeonhwa I mine, Republic of Korea. Miner Deposita 27(1):58–65. https://doi.org/10.1007/BF00196081

Kretschmar U, Scott SD (1976) Phase relations involving arsenopyrite in the system Fe–As–S and their application. Can Miner 14(3):364–386

Lan JB, Liu YP, Ye L, Zhang Q, Wang DP, Su H (2016) Geochemistry and age spectrum of late yanshanian granites from Laojunshan area, southeastern Yunnan Province, China. Acta Miner Sin 36(4):441–454. https://doi.org/10.16461/j.cnki.1000-4734.2016.04.001

Large RR, Danyushevsky L, Hollit C, Maslennikov V, Meffre S, Gilbert S, Bull S, Scott R, Emsbo P, Thomas H, Singh B, Foster J (2009) Gold and trace element zonation in pyrite using a laser imaging technique: implications for the timing of gold in orogenic and carlin-style sediment-hosted deposits. Econ Geol 104(5):635–668. https://doi.org/10.2113/gsecongeo.104.5.635

Lee M, Shin D, Yoo B, Im H, Pak S, Choi S (2019) LA-ICP-MS trace element analysis of arsenopyrite from the Samgwang gold deposit, South Korea, and its genetic implications. Ore Geol Rev 114:103147. https://doi.org/10.1016/j.oregeorev.2019.103147

Lentz DR (2002) Sphalerite and arsenopyrite at the Brunswick no. 12 massive-sulfide deposit, Bathurst camp, new Brunswick: Constraints on P–T evolution. Can Miner 40(1):19–31. https://doi.org/10.2113/gscanmin.40.1.19

Li XH, Liu DY, Sun M, Li WX, Liang XR, Liu Y (2004) Precise Sm–Nd and U–Pb isotopic dating of the supergiant Shizhuyuan polymetallic deposit and its host granite. SE China Geol Mag 141(2):225–231. https://doi.org/10.1017/s0016756803008823

Li XF, Huang C, Wang CZ, Wang LF (2016) Genesis of the huangshaping W–Mo–Cu–Pb–Zn polymetallic deposit in southeastern Hunan Province, China: constraints from fluid inclusions, trace elements, and isotopes. Ore Geol Rev 79:1–25. https://doi.org/10.1016/j.oregeorev.2016.04.023

Li WS, Ni P, Pan JY, Wang GG, Chen LL, Yang YL, Ding JY (2018) Fluid inclusion characteristics as an indicator for tungsten mineralization in the Mesozoic Yaogangxian tungsten deposit, central Nanling district, South China. J Geochem Explor 192:1–17. https://doi.org/10.1016/j.gexplo.2017.11.013

Li JL, Chen ZL, Zhou TF, Gu XX, White NC, Gao HJ (2020) Genesis of the Xiyi Pb–Zn deposit, Yunnan Province, SW China: evidence from trace element and fluid inclusion data. Ore Geol Rev 119:103348. https://doi.org/10.1016/j.oregeorev.2020.103348

Li Y, Yuan F, Jowitt SM, Li XL, Zhou TF, Wang FY, Deng YF (2023) Combined garnet, scheelite and apatite U–Pb dating of mineralizing events in the Qiaomaishan Cu–W skarn deposit, eastern China. Geosci Front 14(1):101459. https://doi.org/10.1016/j.gsf.2022.101459

Li HY, Mao JW, Sun YL, Zou XQ, He HL, Du AD (1996) Re–Os isotopic chronology of molybdenites in the Shizhuyuan polymetallic tungsten deposit, southern Hunan. Geol Rev 42(3):261–267. https://doi.org/10.16509/j.georeview.1996.03.011. (**in Chinese with English abstract**)

Li Y (2014) A study of the metallogenesis of the Zhuxi W-(Cu) polymetallic deposit, Jiangxi province. China (PhD dissertation). University of Geosciences, Beijing (**in Chinese with English abstract**).

Liu YS, Hu ZC, Gao S, Günther D, Xu J, Gao CG, Chen HH (2008) In situ analysis of major and trace elements of anhydrous minerals by LA-ICP-MS without applying an internal standard. Chem Geol 257(1–2):34–43. https://doi.org/10.1016/j.chemgeo.2008.08.004

Liu YP, Li ZX, Ye L, Tan HQ (2011) Ar–Ar chronology of tungsten mineralization in Laojunshan ore concentration area, southeast Yunnan. Acta Miner Sin 31(S1):617–618 (**in Chinese**)

Liu YB, Mo XX, Zhang D, Que CY, Di YJ, Pu XM, Cheng GS, Ma HH (2014) Petrogenesis of the late cretaceous granite discovered in the Laojunshan region, southeastern Yunnan Province. Acta Petrol Sin 30(11):3271–3286 (**in Chinese with English abstract**)

Liu MJ, Yang GS, Chen AB, Wen HJ, Yan YF, Du SJ, Li JK, Yang XY (2023) Genesis of the Marka Pb–Zn–W deposit in southeastern Yunnan: constraints from sphalerite Rb–Sr dating, cassiterite U–Pb dating and in situ S, Pb isotopes of sulfide. Acta Petrol Sin 39(6):1861–1879. https://doi.org/10.18654/1000-0569/2023.06.17. (**in Chinese with English abstract**)

Long ZY, Yu XY, Zheng YY (2021) Ore formation of the Dayakou emerald deposit (Southwest China) constrained by chemical and boron isotopic composition of tourmaline. Ore Geol Rev 135:104208. https://doi.org/10.1016/j.oregeorev.2021.104208

Lu HZ, Liu Y, Wang C, Xu Y, Li H (2003) Mineralization and fluid inclusion study of the Shizhuyuan W–Sn–Bi–Mo–F skarn deposit, Hunan Province, China. Econ Geol 98(5):955–974. https://doi.org/10.2113/gsecongeo.98.5.955

Ma LY, Lu YF, Qu WJ, Fu JM (2007) Re–Os isotopic chronology of molybdenites in Huangshaping lead-zinc deposit, southeast Hunan, and its geological implications. Miner Depos 26(4):425–431 (**in Chinese with English abstract**).

Maslennikov VV, Maslennikova SP, Large RR, Danyushevsky LV (2009a) Study of trace element zonation in vent chimneys from the Silurian Yaman-Kasay volcanichosted massive sulfide deposit (southern Urals, Russia) using laser ablationinductively coupled plasma mass spectrometry (LA-ICPMS). Econ Geol 104:1111–1141. https://doi.org/10.2113/gsecongeo.104.8.1111

Maslennikov VV, Maslennikova SP, Large RR, Danyushevsky LV (2009b) Study of trace element zonation in vent chimneys from the Silurian yaman-kasy volcanic-hosted massive sulfide deposit (southern urals, Russia) using laser ablation-inductively coupled plasma mass spectrometry (LA-ICPMS). Econ Geol 104(8):1111–1141. https://doi.org/10.2113/gsecongeo.104.8.1111

Mirnejad H, Simonetti A, Molasalehi F (2011) Pb isotopic compositions of some Zn–Pb deposits and occurrences from Urumieh-Dokhtar and Sanandaj-Sirjan zones in Iran. Ore Geol Rev 39(4):181–187. https://doi.org/10.1016/j.oregeorev.2011.02.002

Ni P, Pan JY, Han L, Cui JM, Gao Y, Fan MS, Li WS, Chi Z, Zhang KH, Cheng ZL, Liu YP (2023) Tungsten and tin deposits in South China: temporal and spatial distribution, metallogenic models and prospecting directions. Ore Geol Rev 157:105453. https://doi.org/10.1016/j.oregeorev.2023.105453

Nie LQ, Zhou TF, White N, Zhang LJ, Olin P, Meffre S (2021) Textures, trace elements and Pb isotopes of pyrite from the Donggushan tungsten polymetallic deposit, Eastern China: deciphering the source of a skarn tungsten polymetallic deposit. Ore Geol Rev 133:104077. https://doi.org/10.1016/j.oregeorev.2021.104077

Ohmoto H (1972) Systematics of sulfur and carbon isotopes in hydrothermal ore deposits. Econ Geol 67(5):551–578

Pan XF, Hou ZQ, Zhao M, Li Y, Ouyang YP, Wei J, Yang YS (2020) Fluid inclusion and stable isotope constraints on the genesis of the world-class Zhuxi W(Cu) skarn deposit in South China. J Asian Earth Sci 190:104192. https://doi.org/10.1016/j.jseaes.2019.104192

Paton C, Hellstrom J, Paul B, Woodhead J, Hergt J (2011) Iolite: freeware for the visualisation and processing of mass spectrometric data. J Anal at Spectrom 26(12):2508–2518. https://doi.org/10.1039/C1JA10172B

Peng JT, Zhou MF, Hu RZ, Shen NP, Yuan SD, Bi XW, Du AD, Qu WJ (2006) Precise molybdenite Re–Os and mica Ar–Ar dating of the Mesozoic Yaogangxian tungsten deposit, central Nanling district, South China. Miner Deposita 41(7):661–669. https://doi.org/10.1007/s00126-006-0084-4

Peters T (1987) Hydrothermal alteration of a variscian granite, magmatic autometasomatism and fault related vein metasomatism. In: Chemical transport in metasomatic processes. Springer, pp 577–590. https://doi.org/10.1007/978-94-009-4013-0_21

Poblete JA, Dirks PHGM, Chang ZS, Huizenga JM, Griessmann M, Hall C (2021) The watershed tungsten deposit, northeast Queensland, Australia: permian metamorphic tungsten mineralization overprinting carboniferous magmatic tungsten. Econ Geol 116(2):427–451. https://doi.org/10.5382/econgeo.4791

Poulin RS, McDonald AM, Kontak DJ, McClenaghan MB (2016) On the relationship between cathodoluminescence and the chemical composition of scheelite from geologically diverse ore-deposit environments. Can Miner 54(5):1147–1173. https://doi.org/10.3749/canmin.1500023

Qi HW, Hu RZ, Wang XF, Qu WJ, Bi XW, Peng JT (2012) Molybdenite Re–Os and muscovite ^{40}Ar/^{39}Ar dating of quartz vein-type W-Sn polymetallic deposits in Northern Guangdong, South China. Miner Deposita 47(6):607–622. https://doi.org/10.1007/s00126-012-0406-7

Que CY, Zhang D, Di YJ, Bi MF, Huang KW, Xu JZ, Liu YB, Li XZ, Zu SY, Fan ZZ, Wang S (2014) Ore-controlling characteristics of tungsten deposits in the Nanwenhe Saxi area and deep prospecting breakthrough. Earth Sci Front 21(2):286–300 (**in Chinese with English abstract**). https://doi.org/10.13745/j.esf.2014.02.021

Que CY (2016) Study on tungsten metallogenic system and prospecting direction in the Nanwenhe-Saxi area of Malipo, Yunnan (Ph.D Dissertation). China University of Geosciences, Beijing (**in Chinese with English abstract**)

Reich M, Kesler SE, Utsunomiya S, Palenik CS, Chryssoulis SL, Ewing RC (2005) Solubility of gold in arsenian pyrite. Geochim Cosmochim Acta 69(11):2781–2796. https://doi.org/10.1016/j.gca.2005.01.011

Reich M, Deditius A, Chryssoulis S, Li JW, Ma CQ, Parada MA, Barra F, Mittermayr F (2013) Pyrite as a record of hydrothermal fluid evolution in a porphyry copper system: a SIMS/EMPA trace element study. Geochim Cosmochim Acta 104:42–62. https://doi.org/10.1016/j.gca.2012.11.006

Román N, Reich M, Leisen M, Morata D, Barra F, Deditius AP (2019) Geochemical and micro-textural fingerprints of boiling in pyrite. Geochim Cosmochim Acta 246:60–85. https://doi.org/10.1016/j.gca.2018.11.034

Sheng X, Zhang D, Que CY, Bi MF, Di YJ, Zu SY, Ma HH (2023) Sources and evolution of ore-forming fluids from the Saxi tungsten-beryllium deposit in southeastern Yunnan Province: evidence from fluid inclusions and H–O isotopes. Bull Geol Sci Technol 42(1):158–273 (**in Chinese**). https://doi.org/10.19509/j.cnki.dzkq.2022.0103

Sheng X (2016) Study on geological characteristics and ore-forming fluids of Saxi tungsten deposit in Laojunshan, Southeast Yunnan Province. China (PhD dissertation). University of Geosciences, Beijing (**in Chinese with English abstract**)

Shi HZ, Zhang LK, Fan WY, Lin FC (2015) Metallogenic model of Laojunshan area Nanyangtian scheelite deposit in SE Yunnan. China Tungsten Ind 30(2):1–6 (**in Chinese with English abstract**). https://doi.org/10.3969/j.issn.1009-0622.2015.02.001

Sirbescu MC, Nabelek PI (2003) Crystallization conditions and evolution of magmatic fluids in the Harney Peak Granite and associated pegmatites, Black Hills, South Dakota: evidence from fluid inclusions. Geochim Cosmochim Acta 67(13):2443–2465. https://doi.org/10.1016/S0016-7037(02)01408-4

Soloviev SG, Kryazhev SG, Dvurechenskaya SS (2017) Geology, mineralization, stable isotope, and fluid inclusion characteristics of the Vostok-2 reduced W-Cu skarn and Au–W–Bi–As stockwork deposit, Sikhote-Alin, Russia. Ore Geol Rev 86:338–365. https://doi.org/10.1016/j.oregeorev.2017.02.029

Sun P, Guo PY, Niu YL (2021) Eastern China continental lithosphere thinning is a consequence of paleo-Pacific plate subduction: a review and new perspectives. Earth Sci Rev 218:103680. https://doi.org/10.1016/j.earscirev.2021.103680

Vermeesch P (2018) IsoplotR: a free and open toolbox for geochronology. Geosci Front 9(5):1479–1493. https://doi.org/10.1016/j.gsf.2018.04.001

Wang XJ, Liu YP, Miao YL, Bao T, Ye L, Zhang Q (2014) In situ LA-MC-ICP-MS cassiterite U–Pb dating of Dulong Sn–Zn polymetallic deposit and its significance. Acta Petrol Sin 30(3):867–876 (**in Chinese with English abstract**).

Wang XD, Ni P, Yuan SD, Wu SH (2012) Characteristics of fluid inclusions of the Muziyuan tungsten deposit in Southern Jiangxi Province and their geological implications. Geol China 39(6):1790–1797 (**in Chinese with English abstract**). https://doi.org/10.3969/j.issn.1000-3657.2012.06.024

Wilson SA, Ridley WI, Koenig AE (2002) Development of sulfide calibration standards for the laser ablation inductively-coupled plasma mass spectrometry technique. J Anal at Spectrom 17(4):406–409. https://doi.org/10.1039/B108787H

Wu SH, Mao JW, Yuan SD, Dai P, Wang XD (2018) Mineralogy, fluid inclusion petrography, and stable isotope geochemistry of Pb–Zn–Ag veins at the Shizhuyuan deposit, Hunan Province, southeastern China. Miner Deposita 53(1):89–103. https://doi.org/10.1007/s00126-017-0725-9

Wu YF, Evans K, Hu SY, Fougerouse D, Zhou MF, Fisher LA, Guagliardo P, Li JW (2021) Decoupling of Au and As during rapid pyrite crystallization. Geology 49(7):827–831. https://doi.org/10.1130/g48443.1

Wu Q, Williams-Jones AE, Zhao PL, Yuan SD (2023) The nature and origin of granitic magmas and their control on the formation of giant tungsten deposits. Earth Sci Rev 245:104554. https://doi.org/10.1016/j.earscirev.2023.104554

Xu B, Jiang SY, Hofmann AW, Wang R, Yang SY, Zhao KD (2016) Geochronology and geochemical constraints on petrogenesis of early paleozoic granites from the Laojunshan district in Yunnan Province of South China. Gondwana Res 29(1):248–263. https://doi.org/10.1016/j.gr.2014.12.006

Xue G, Marshall D, Zhang S, Ullrich TD, Bishop T, Groat LA, Thorkelson DJ, Giuliani G, Fallick AE (2010) Conditions for early cretaceous emerald formation at Dyakou, China: Fluid inclusion, Ar–Ar, and stable isotope studies. Econ Geol 105(2):339–349. https://doi.org/10.2113/gsecongeo.105.2.339

Yang JH, Zhang Z, Peng JT, Liu L, Leng CB (2019) Metal source and wolframite precipitation process at the Xihuashan tungsten deposit, South China: Insights from mineralogy, fluid inclusion and stable isotope. Ore Geol Rev 111:102965. https://doi.org/10.1016/j.oregeorev.2019.102965

Yuan HL, Liu X, Chen L, Bao ZA, Chen KY, Zong CL, Li XC, Qiu JW (2018) Simultaneous measurement of sulfur and lead isotopes in sulfides using nanosecond laser ablation coupled with two multi-collector inductively coupled plasma mass spectrometers. J Asian Earth Sci 154:386–396. https://doi.org/10.1016/j.jseaes.2017.12.040

Zartman RE, Doe BR (1981) Plumbotectonics: The model. Tectonophysics 75(1–2):135–162. https://doi.org/10.1016/0040-1951(81)90213-4

Zhang B, Zhang LK, Shi HZ, Chen MH, Liu SS (2012) Rare earth elements geochemical characteristics and its implication for ore genesis in saxi scheelite deposit, southeast Yunnan Province. Geol Miner Resour South China 28(3):232–236 (**in Chinese with English abstract**).

Zhang B, Zhang BH, Zhang LK, Chen MH (2016) Characteristics of ore-forming fluids of the Saxi scheelite deposit, Laojunshan ore concentrated area in southeast Yunnan Province, and its geological significance. Geol Miner Resour South China 32(4):333–342 (**in Chinese with English abstract**).

Zhang XM, Zhang D, Bi MF, Wu GG, Fan ZZ, Que CY, Di YJ, Xue W, Zhou ZG, Bai H (2021) Genesis and geodynamic setting of the Nanyangtian tungsten deposit, SW China: Constraints from structural deformation, geochronology, and S–O isotope data. Ore Geol Rev 138:104354. https://doi.org/10.1016/j.oregeorev.2021.104354

Zhang WL, Hua RM, Wang RC, Li HM, Qu WJ, Ji JQ (2009) New dating of the Piaotang granite and related tungsten mineralization in southern Jiangxi. Acta Geol Sin 83(5):659–670. https://doi.org/10.3321/j.issn:0001-5717.2009.05.007. (**in Chinese**)

Zhao XY, Deng MG, Li WC, Tang YW, Zhang DC, Han SK, Song WB, Zhang QG, Xu JW (2024) In situ U–Pb dating of garnet, vesuvianite, and scheelite from the Nanyangtian tungsten deposit reveals an early cretaceous W mineralization event in Southeast Yunnan, China. Gondwana Res 133:72–90. https://doi.org/10.1016/j.gr.2024.06.002

Zheng YY, Yu XY, Guo HS (2019) Major and trace element geochemistry of dayakou vanadium-dominant emerald from Malipo (Yunnan, China): genetic model and geographic origin determination. Minerals 9(12):777. https://doi.org/10.3390/min9120777

Springer Nature or its licensor (e.g. a society or other partner) holds exclusive rights to this article under a publishing agreement with the author(s) or other rightsholder(s); author self-archiving of the accepted manuscript version of this article is solely governed by the terms of such publishing agreement and applicable law.